Materials Advances

ROYAL SOCIETY OF CHEMISTRY

PAPER

View Article Online
View Journal | View Issue

Cite this: *Mater. Adv.*, 2023, 4, 1062

Photocurrent conversion capability of a 2D WS_2-polyvinyl alcohol matrix and its DFT-based charge carrier dynamics analysis†

Arpit Verma, [a] Anshika Singh, [b] Priyanka Chaudhary, [c] Ravi Kant Tripathi, [d] B. C. Yadav, *[a] Pratima Chauhan[b] and Devesh Kumar[e]

Received 9th October 2022,
Accepted 4th January 2023

DOI: 10.1039/d2ma00962e

rsc.li/materials-advances

In the present research article, we have studied the photodetection mechanism of WS_2 nanosheets embedded in a polyvinyl alcohol matrix. Hydrothermally synthesized nanosheets of WS_2 were embedded in a polyvinyl alcohol (PVOH) matrix by the solution method. The SEM micrographs show the clear incorporation of WS_2 nanosheets in the PVOH matrix. XRD results reveal the hexagonal-type crystal structure of the WS_2 nanosheets with the space group of *P*63/*mmc*. A Tauc plot of the UV-Visible absorption spectrum of the WS_2 PVOH matrix shows the optical band gap energy of 3.51 eV, which is intermediate between those of the WS_2 nanosheets and PVOH matrix. The zeta potentials of the WS_2 nanosheets, PVOH and WS_2 PVOH were found to be −10.60 mV, −4.14 mV and −1.12 mV, respectively. The responsivity and detectivity were found to be 369.13 mA W^{-1} and 5.25 × 10^{11} Jones, respectively, in the photodetection measurement for the WS_2 PVOH metallopolymer. The density functional studies show that upon the incorporation of the WS_2 nanosheets into the PVOH matrix, the HOMO–LUMO energy gap significantly decreases. Electronic properties such as electron affinity, ionization potential, chemical hardness, and amount of charge transfer concluded based on DFT also support the experimental results.

1. Introduction

Photon to electricity conversion materials are employed in any application that calls for the detection of light at a specific wavelength, including imaging, spectroscopy, remote sensing, solar cells and others.[1,2] The great majority of silicon based photodetectors currently in use, operate in the visible or near-infrared region and have peak operating wavelengths greater than 500 nm. Wide ranges of mechanical, electrical, and optoelectronic characteristics of two-dimensional materials, including transition metal dichalcogenides (TMDCs), are currently the subject of intense research. The 2D material that has received the greatest attention is graphene, which led to the field's expansion to other 2D materials including TMDCs.[3–5] Next-generation devices can function more effectively due to the special properties of 2D materials, including their ultrathin planar structure, strong electron–hole confinement, and layer-dependent variable bandgap. These characteristics make it possible to create devices that are smaller, more flexible, and more efficient.[6–8] In graphene, the absence of a band gap, despite its exceptional carrier mobility, restricts its use in electronics. Due to their unique features, TMDCs have received a lot of interest and have been suggested as prospective candidate for photonic and optoelectronic devices.[9–11]

In contrast to other two-dimensional materials, WS_2 demonstrates unique characteristics including conductivity, which makes it ideal for contacts and interconnections, mechanical strength, a very high elastic modulus, high thermal stability, and excellent mobility. Graphene is the most researched two-dimensional material.[12–14] The ability to directly fabricate heterojunctions made up of several 2D materials is made possible by the same weak van der Waals interactions that make it simple to separate atomically thin sheets from stacked solids.[15–19] The next generation of optoelectronic and nanoscale electronic devices will be built using heterostructures based on these TMDCs.[20,21] 2D materials may be coupled with other electronic materials including zero-dimensional quantum dots (0D), one-dimensional nanotubes (1D), and polymers

[a] *Nanomaterials and Sensors Research Laboratory, Department of Physics, Babasaheb Bhimrao Ambedkar University, Lucknow-226025, UP, India. E-mail: balchandra_yadav@rediffmail.com*
[b] *Advanced Nanomaterials Research Laboratory, U. G. C. Centre of Advanced Studies, Department of Physics, University of Allahabad, Prayagraj-211002, India*
[c] *Department of Materials Engineering, Ming Chi University of Technology, New Taipei City, 24301, Taiwan*
[d] *Department of Physics, Lal Bahadur Shastri Smarak Post Graduate College, Maharajganj-273161, UP, India*
[e] *Department of Physics, Siddharth University, Kapilvastu, Uttar Pradesh 272202, India*

† Electronic supplementary information (ESI) available. See DOI: https://doi.org/10.1039/d2ma00962e

(3D) to create mixed-dimensional van der Waals (vdW) heterostructures with new device properties.[22–24] Numerous studies have also been done on certain other characteristics, such as transparency, stretchability, and self-healing.[25,26]

Polymer materials are potential materials for a new generation of photodetectors because of their inherent flexibility, solution processability, large-area preparation, and tunable molecular structure. This is accomplished by various molecular design methodologies and novel device designs.[27] Thick-film photoactive layers are preferred in all-polymer photodetectors to obtain high detectivity since they can efficiently reduce the dark current density. However, if the photoactive layer of the film is too thick, it causes greater recombination loss, which reduces responsiveness.[28,29] Impact ionization cannot happen in organic photodetectors like in inorganic avalanche photodiodes because the exciton binding energy of organic semiconductor materials is roughly 0.1–1.4 eV, which is three orders higher than that of inorganic semiconductor materials[28] and trap-assisted carrier tunneling effects have been primarily responsible for helping to identify the working mechanism of organic photodetectors.[30] In this research, the photo to current conversion capability is tested in terms of the performance parameters such as responsivity (R), detectivity (D), external quantum efficiency (EQE), linear dynamic range (LDR), and noise equivalent power (NEP). Due to the presence of the W atom in the WS_2 and the –OH functional group in the PVOH matrix, in the metallopolymeric system, there is an interaction between them. This is also studied by the density functional theory approach for insight into the charge carrier dynamics.

2. Experimental section

2.1 Materials used

Sodium tungstate dihydrate ($Na_2WO_4{\cdot}2H_2O$, Fisher Scientific, >99.5%), thiourea (NH_2CSNH_2, SDFCL, >99), polyvinyl alcohol (Sigma Aldrich, >99.9%), *N*-methyl-2-pyrrolidone [C_5H_9NO, Merck, >99.3%], ethanol [C_2H_5OH], and acetone [CH_3COCH_3] of Fisher Scientific India.

2.2 Synthesis of 2D WS_2 nanosheets

In a typical synthesis technique, 30 mL of double-distilled water was used to make a 0.3 M solution of sodium tungstate dihydrate, which was then stirred for 1 hour at 90 °C. Following that, a 0.6 M solution of thiourea was prepared in 30 mL of double-distilled water. The thiourea solution was then added to a tungsten precursor solution and the mixture was again stirred at 150 °C for 3 hours at a speed of 500 rpm (relation (1b)). The mixture was then cooled to room temperature and titrated with HCl while being constantly stirred until a brown precipitate developed. The final pH was adjusted to 1 because at this pH value most of the material precipitated. Then, this solution was put into a 100 mL autoclave that was lined with Teflon. The autoclave was placed in an oven set at 150 °C for 5 hours. This solution was removed from the oven after natural cooling and centrifuged three times at 3500 rpm with distilled water. Additionally, this powder was dried in a programmable oven at 200 °C (relation (1c)).

$$(NH_2)_2CS + 2H_2O \rightarrow 2NH_3 + CO_2 + H_2S \quad (1a)$$

$$Na_2WO_4{\cdot}2H_2O + 3H_2S \rightarrow WS_3 + 2NaOH + 4H_2O \quad (1b)$$

$$WS_3 \rightarrow WS_2(\text{black}) + S \quad (1c)$$

2.3 Incorporation of WS_2 nanosheets into the PVOH matrix

In the first step of the synthesis, WS_2 was dissolved in *N*-methyl pyrrolidone and ultra-sonicated for 5 hours in an ultrasonic bath for further breaking the WS_2 sheets into smaller sheets, as shown in Fig. 1 (step 1). After ultra-sonication, these WS_2 nanosheets were centrifuged at 3500 rpm to collect them. These

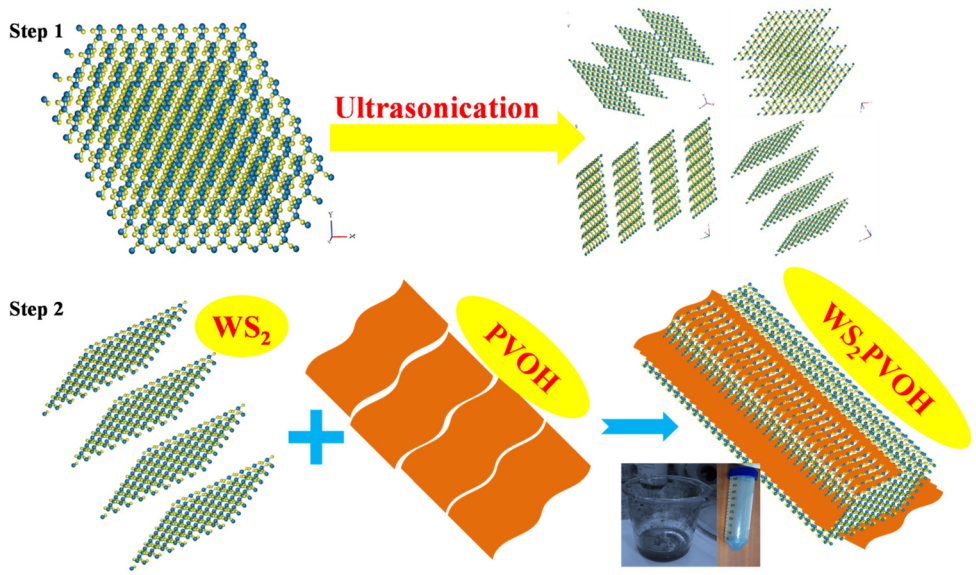

Fig. 1 Preparation procedure for the WS_2 PVOH metallopolymer.

bottom collected WS_2 nanosheets were dried at 80 °C in a programmable oven. The process of incorporation of WS_2 sheets into the PVOH matrix is depicted in Fig. 1 (step 2). In 50 mL of double distilled water 5 g of polyvinyl alcohol was dissolved at 80 °C on a magnetic stirrer. When all the PVOH dissolved in distilled water 1 g of previously synthesized WS_2 nanosheets was dropped into the PVOH solution and this solution was continuously stirred up to 5 hours. This WS_2 nanosheet embedded PVOH matrix was used for further analysis.

3. Results and discussion

3.1 Surface morphological investigation

Scanning electron microscopy (SEM) was used to examine the morphology of the samples. Fig. 2(a–c) displays the SEM pictures of the WS_2 hexagonal nanosheets. It is evident from Fig. 2(b) and (c) that there are several clusters of nanosheets, whereas Fig. 2(c) clearly shows hexagon-shaped sheets. It can be seen that nanosheets incorporated in the PVOH matrix are essentially monodispersed, loosely stacked, and have a width between 100 and 500 nm and a thickness of 10 nm. Energy dispersive X-ray spectroscopy (EDS) was used to confirm the elemental composition of the as-prepared materials. In the EDS spectrum of WS_2, W and S elements are observed with an atomic percentage of 30.38 and 69.62% respectively, as shown in Fig. 2(g). In the WS_2 PVOH matrix, W and S were found to be 2.42% and 4.30% whereas C and O are also present with an atomic percentage of 74.98% and 18.30%, respectively, as depicted in Fig. 2(h).

3.2 Raman spectroscopic analysis

Raman spectroscopy is frequently used to ascertain the number of layers and other important characteristics of layered 2D materials. The point group corresponds to D_{6h} for bulk, D_{3h} for an odd number of layers, and D_{3d} for an even number of layers.[31] The crystal structure of 2H-WS_2 belongs to the D_{6h}^4 point group. The following relation (2) describes the zone center phonons' irreducible representations.[32]

$$\Gamma = A_{1g} + 2A_{2u} + B_{1u} + 2B_{2g} + E_{1g} + 2E_{1u} + E_{2u} + 2E_{2g} \quad (2)$$

The E_{2g}^1 mode involves in-plane displacement of transition metal and chalcogen atoms, whereas the A_{1g} mode only involves chalcogen atoms and is an out-of-plane vibration.[33] E_{2g}^2 is a shear mode that manifests at very low frequencies and describes the vibration of two stiff layers rubbing against one another. The back-scattering Raman setup forbids the E_{1g} mode, an in-plane vibration of solely the chalcogen atoms.[33,34] Table 1 demonstrates how the peaks are shifting. The strongest second-order Raman peak, the 2LA(M) mode at

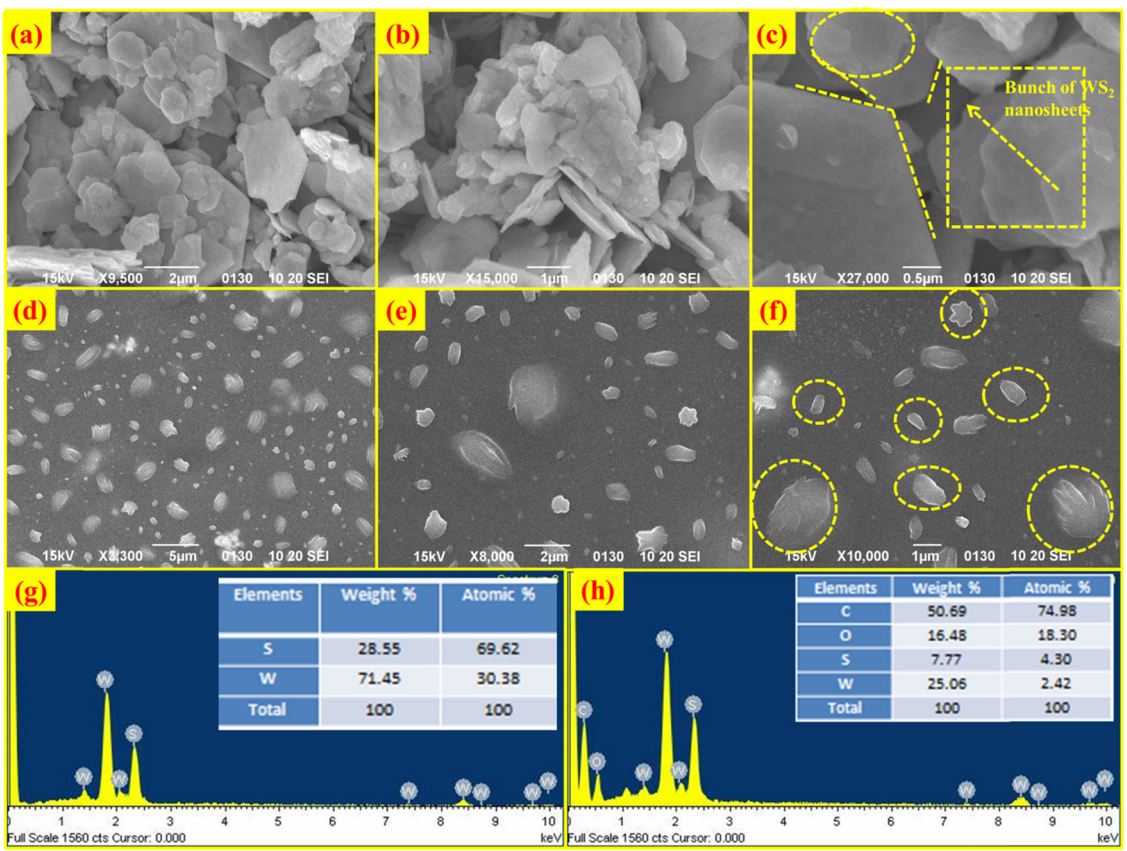

Fig. 2 Scanning electron micrographs of WS_2 nanosheets at (a) 2 μm, (b) 1 μm and (c) 0.5 μm, scanning electron micrographs of WS_2 nanosheets embedded in a PVOH matrix at (d) 5 μm, (e) 2 μm and (f) 1 μm, (g) EDS spectrum of WS_2 nanosheets and (h) EDS spectrum of WS_2 PVOH.

Table 1 Raman modes in WS_2 nanosheets and WS_2 PVOH

S. no.	WS_2 nanosheets (cm^{-1})	WS_2 PVOH (cm^{-1})	$\Delta\omega$ (cm^{-1})
1.	299.089	300.712	1.623
2.	332.619	332.975	0.356
3.	350.718	351.880	1.162
4.	358.924	359.851	0.927
5.	423.748	424.414	0.666

350.718 cm^{-1}, is nearly twice as strong as the first-order $A_{1g}(\Gamma)$ such as shown in Fig. 3(a). However, at 358.924 cm^{-1}, the second-order 2LA(M) mode overlaps with the first-order $E^1{}_{2g}(\Gamma)$ mode.

3.3 Structural analysis

To evaluate the structure, these nanomaterials were analyzed by X-ray diffraction (XRD) technique. The XRD pattern of the WS_2 nanosheets is shown in Fig. 4(a), with the (*hkl*) planes of (002), (004), (100), (101), (103), (006), (105), (110), (112), (108) and (118) found at the 2θ angles of 14.22°, 28.79°, 32.66°, 33.42°, 39.43°, 43.85°, 49.59°, 58.32°, 60.39°, 68.91° and 88.42°, respectively. In the diffraction pattern of PVOH as in Fig. 4(b), the diffraction peaks at 19.57°, 22.74° and 40.52° correspond to the (101), (200) and (111) reflection planes. This crystalline peak of PVOH is also similar to some previous results.[35] The –OH group contributes to the crystallinity of PVOH, a semi-crystalline polymer. These crystalline areas, which are dispersed randomly throughout the polymer, are crucial to the polymer's chemical and physical characteristics. The XRD pattern of PVOH is distinguished by the chains in a trans-planar conformation packed in a monoclinic unit cell, according to the PVOH's diffraction profile.[36] The PVOH main chain has enough –OH groups to create potent intra- and intermolecular hydrogen bonds. Because of its high crystallinity, WS_2 is extremely dominating in the overall pattern, as seen by the XRD pattern of WS_2 PVOH in Fig. 4(c). The Scherrer formula (relation (3)) was used to compute the average crystallite size.

$$L = \frac{k\lambda}{\beta \cos\theta} \tag{3}$$

where k is the Scherrer constant, β is the full width and half maximum, and Cu k_α is the wavelength (λ = 0.15406 nm). The WS_2 nanosheets' average crystallite size was found to be 32.40 nm.

3.4 UV-Visible absorption spectroscopy

The UV-Visible absorption spectra for WS_2 nanoflakes, PVOH, and WS_2 PVOH are shown in Fig. 5(a) in the range of 200 to 750 nm. The absorption coefficient of all samples was calculated by the Beer–Lambert law such as given in relations (4) and (5).

$$I = I_0 e^{-\alpha t} \tag{4}$$

$$\alpha = \frac{2.303\,A}{t} \tag{5}$$

where I and I_0 are the optical intensities at the moment and the initial intensity, α is the absorption coefficient, t is the cuvette's thickness, and A is the absorption. The Tauc plot technique was used to determine the optical band gap energy of the materials, and it is presented in relation (6).

$$\alpha h\nu = A(h\nu - E_g)^n \tag{6}$$

The exponent n is used to express the type of band transition, where n = 2 and 3 respectively denote indirect permitted and indirect forbidden transitions, while n = 1/2 and 3/2 respectively denote direct permitted and direct prohibited transitions, A is a constant and ν denotes the transition frequency. The optical band gap was found by projecting the straight line segment of the $(\alpha h\nu)^2$ against hυ curves to zero.[37,38] The predicted band gaps of the as-prepared materials were determined to be 1.94 eV for WS_2 nanosheets and 4.51 eV for PVOH, whereas 3.51 eV for WS_2 PVOH as shown in Fig. 5(b).

3.5 Dynamic light scattering analysis

When suspended in a liquid, nanoparticles scatter light in a manner proportional to the sixth power of their radii.[39] When using DLS, the autocorrelation function is calculated using the mono-exponential relation (7) and the variations in scattered light intensity are correlated against short decay periods.[40,41]

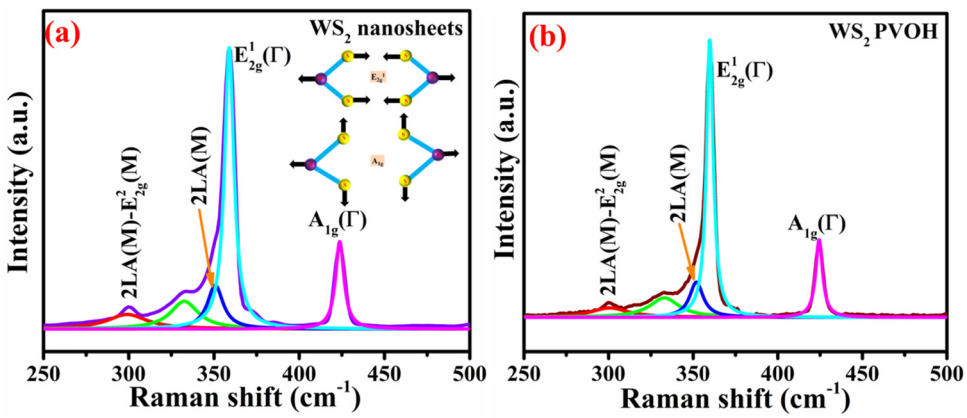

Fig. 3 (a) Raman spectrum of WS_2 nanosheets (inset: Raman modes). (b) Raman spectrum of WS_2 PVOH.

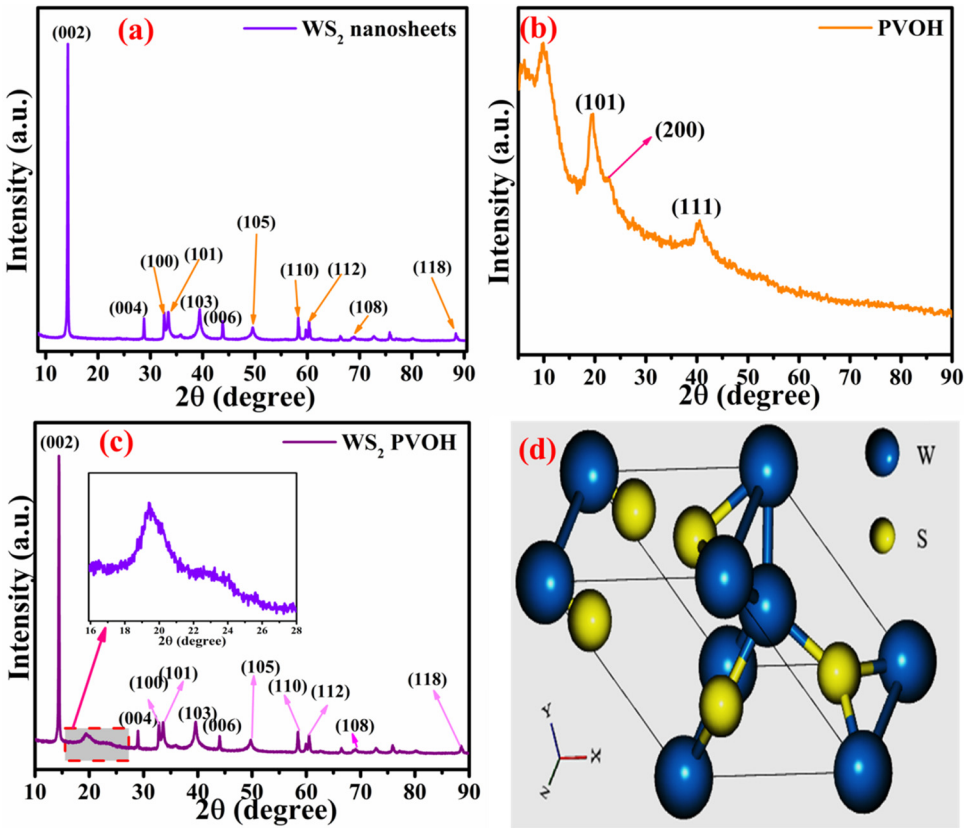

Fig. 4 X-Ray diffraction pattern of (a) WS_2 nanosheets, (b) PVOH and (c) WS_2 PVOH. (d) Crystal unit cell of WS_2.

$$G(\tau) = 1 + be^{-2D_t q^2 \tau} \quad (7)$$

where q is the scattering vector, D_t is the translational diffusion coefficient, and b is an instrument-dependent constant. The Stokes–Einstein relation (8) links this translational diffusion coefficient to the hydrodynamic radius (R_H) of solid spherical particles.[42]

$$D_t = \frac{k_B T}{6\pi\eta R_H} \quad (8)$$

From the analysis of the as-prepared materials, the distribution of nanoparticles is presented in Fig. 5(c). However, in PVOH, this size distribution is dominated in a wide range between 70 and 300 nm. The distribution of WS_2 nanosheets was found to be 100–200 nm. The WS_2 PVOH material's particle size distribution lies between these two counterparts which is in the range of 175–275 nm.

3.6 Zeta potential analysis

The electrified double layer of electrophoretically movable particles and the layer of dispersant around them have a potential difference at the sliding plane known as the zeta potential. Zeta potential measurements are highly associated with the colloid's stability. Zeta potential levels are categorized as very unstable, generally stable, moderately stable, and highly stable, respectively, between the ranges of 0–10 mV, 10–20 mV, 20–30 mV, and 30 mV.[42,43] The WS_2 nanosheets' zeta potential value discovered to be −10.60 mV, showing that they are relatively stable in their solvent, as opposed to PVOH and WS_2 PVOH, whose zeta values were detected to be −4.14 mV and −1.12 mV and displayed in Fig. 5(d). These two dispersant solutions are very unstable, as shown by Fig. 5(d), which indicates that they have a tendency to aggregate.

3.7 Photodetection analysis and their mechanism

Fig. 6 displays the schematic representation of the photodetection measurement set-up, which consists of a light source of the wavelength centered at 365 nm. This setup is connected with an electrometer and the computer through the GPIB port. The band diagram presented in Fig. 6 shows that under the ambient atmospheric conditions, oxygen molecules adsorbed on the surface of the materials in the form of O^{2-}, taking an electron from the conduction band. Thus a depletion region is formed between the material and oxygen species. Upon illumination these oxygen species are removed from the surface of the materials, so the depletion width is reduced and a higher level of photocurrent is observed. In the photoconduction process, instead oxygen adsorption/desorption mechanisms along with exciton generation, transportation and collection are also responsible. Such as under illumination, electron–hole pairs are generated in the materials and under the application of small potential drift these excitons move towards the respective electrodes and are collected on the electrodes, which is exhibited as increased photocurrent in the external circuit. Our photodetector devices have a metal–semiconductor–metal (MSM)-based coplanar device structure, where silver (Ag) is

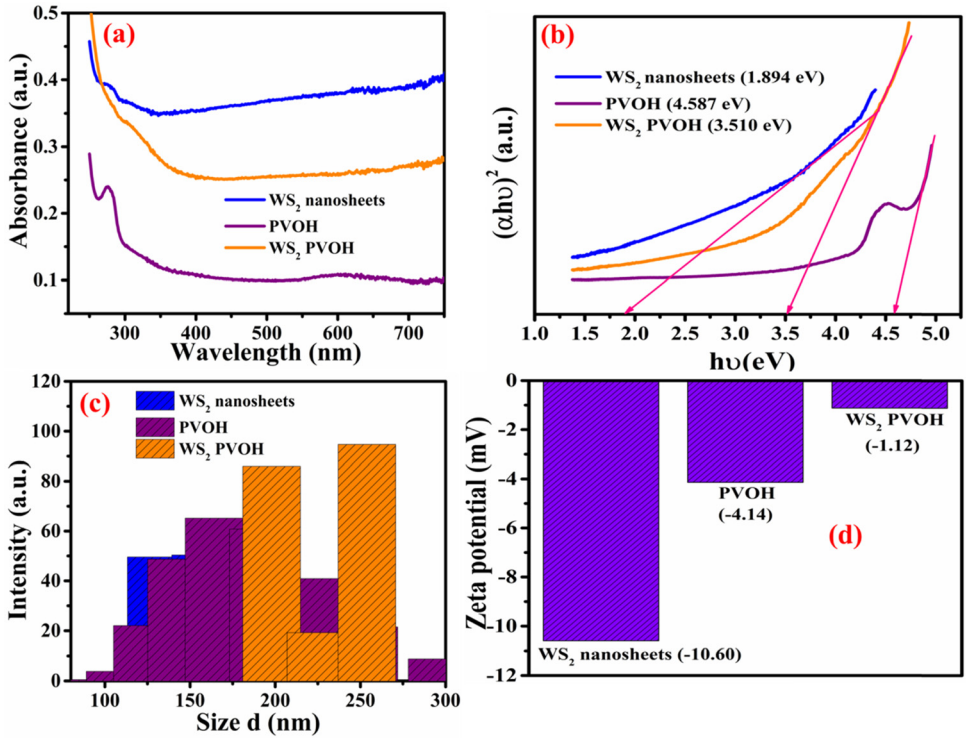

Fig. 5 (a) UV-Visible absorption spectrum of WS_2 nanosheets, PVOH and WS_2 PVOH. (b) Tauc plot for WS_2 nanosheets, PVOH and WS_2 PVOH. (c) Dynamic light scattering spectrum of WS_2 nanosheets, PVOH and WS_2 PVOH. (d) Zeta potential plot for WS_2 nanosheets, PVOH and WS_2 PVOH.

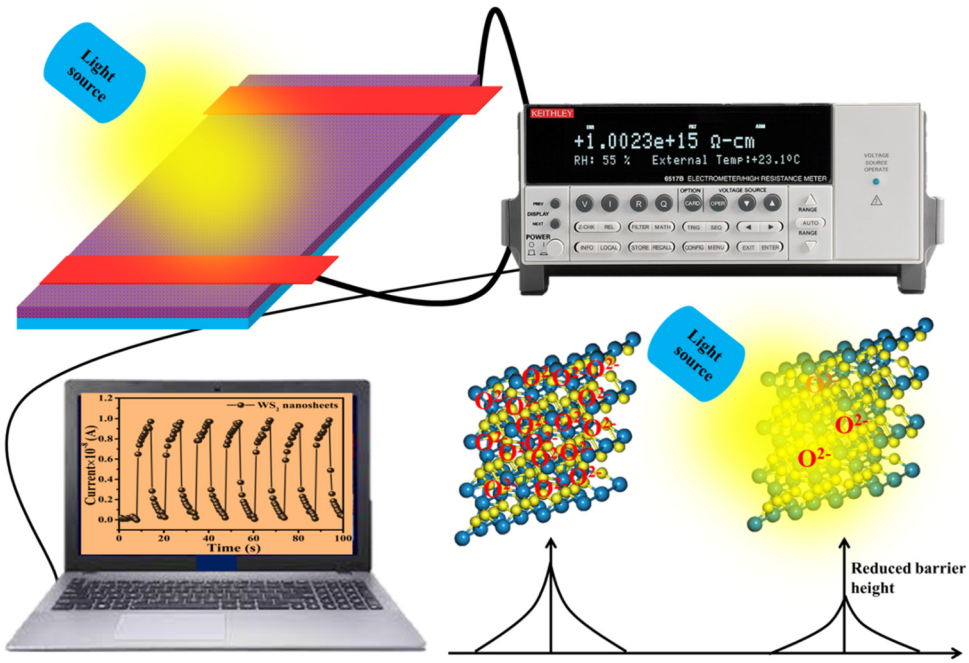

Fig. 6 The experimental set-up is depicted schematically, along with the corresponding band diagram under dark and illuminated conditions.

used for symmetrical electrodes. There is a need to enhance photodetector performance parameters such as responsivity, detectivity, noise equivalent power and external quantum efficiency because their usability in diverse fields needs different specifications. For more accurate and precise measurements of light, a highly responsive photodetector must be chosen, whereas for the detection of weak light signals, a high detectivity and low NEP photodetector device is needed. There are two

approaches to increase the sensitivity of photodetectors: by improving the external quantum efficiency and by reducing the dark current density. One of the most crucial methods for increasing EQE and producing high-sensitivity photodetection is the photomultiplication (PM) effect.[44] Since the exciton binding energies of organic semiconductor materials are in between 0.1 and 1.4 eV, and are roughly three orders more than those of inorganic semiconductors, impact ionization cannot take place in organic photomultiplication as it can in inorganic photodiodes. Instead, carrier tunneling events facilitated by traps have been used to investigate how organic PM photodetectors operate.[28,45] The EQE of the majority of organic MSM photodetectors is substantially higher than 100% owing to the carrier tunneling effect that is helped by traps.[46,47] When the Fermi energy level of the metal electrode is higher than that of the hybrid material, the required Schottky band bending without bias occurred in organic-inorganic semiconductors with a lot of electron traps.[28,48] Ag, Al, and Mg electrodes must be used to create band bending because of their low work functions. Photo-generated electrons are captured by electron traps when exposed to light and travel toward the Schottky junction in the presence of a biased electric field from the electrode to the semiconductor.[28,49] As a result of the incoming electrons narrowing the Schottky junction there and boosting the internal electric field's strength, holes are then able to tunnel through the junction and inject into the hybrid semiconductor from the outside circuit, resulting in current multiplication.[50] A high-frequency detector that uses an insulating layer to exclude ambient light has recently been developed in photodetectors. The narrowband detector requirement is a further invention that uses ineffective charge transport to produce a sizable peak in external quantum efficiency near the optical absorption edge of active layers.[51] Different material-based photodetector devices are presented in Table 2 for the comparison of these results. The linear Ohmic properties are shown in Fig. 7(a–c), which denotes the emergence of Ohmic connections between the material and electrodes. The photodetector device based on WS_2 PVOH shows a high photocurrent but at the same time is less effective towards the intensity, which may be due to the presence of WS_2 traps in the PVOH matrix. According to Fig. 7(d), it is also evident that WS_2 PVOH exhibits a higher photocurrent than pure WS_2 nanosheets and PVOH.

Fig. 8 displays the transient photoresponse behavior of all the as-prepared devices. From Fig. 8(a) the transient photoresponse of the WS_2 nanosheets exhibited a very fast and stable photoresponse, which is attributed to the two-dimensional nature with lower recombination centers. Whereas the photoresponse of WS_2 PVOH shows some level of enhancement in the current after some on/off cycles; the main reason behind this is that after interaction with light some thermally excited carriers were also generated, which contributed to the photocurrent but at the same time reduced the stability of the device. The WS_2 PVOH device was also checked for long term stability up to 600 s such as presented in Fig. 8(d), which also exhibits the fluctuating nature of the device where after some time, the current decreases and then increases within some threshold limit. This degrading behavior of the device was also confirmed by the photodetection measurement of the pure PVOH device as shown in Fig. 8(f), which exhibited that after each measurement the photocurrent degraded, which is attributed to the fact that PHOV is more thermally responsive as compared to photons, whereas WS_2 nanosheets are photoresponsive. Upon combining these two materials we found a photodetector device, with high photocurrent and long-term stability. Relation (9) defines the responsivity of the photodetector device as the production of photocurrent from the noise level for each incident photon per unit area.[52,53] The calculated responsivity of the photodetector devices is found to be 5.24 mA W^{-1} and 9.22 mA W^{-1} for WS_2 nanosheets and PVOH, respectively, whereas the responsivity for the WS_2 PVOH nanohybrid was significantly enhanced and found to be 369.13 mA W^{-1}, which is due to the fact that upon incorporating the WS_2 sheets into the PVOH matrix, the photocurrent rises at lower potentials. This result is very close to the previously reported PVA/CQD-based device responsivity of 0.26 A W^{-1}.[54] According to relation (10), the gain of a photoconductor is equal to the minority carrier recombination lifetime divided by the time the carriers need to travel across the semiconductor between the two contacts of the device. Given that the transit time is significantly less than the recombination lifetime, a photoconductor will inevitably experience a considerable gain. The photogenerated carriers have numerous opportunities to go through the circuit before recombination because of the short transit time, which results in many times more photoexcited carriers. This is how the gain physically explains itself. The gain for the WS_2 PVOH device is 1.25×10^9, which is significantly higher than the gain of WS_2 of 1.78×10^7

Table 2 Different materials-based photodetector devices

Material	R (A W^{-1})	D (Jones)	P_{inc} (μW cm^{-2})	EQE (%)	Ref.
WS_2–PVOH	0.36	5.25×10^{11}	50	125.15	Present work
PVA/CQD	0.267	—	5×10^3	158	54
Polyaniline–WSe_2	0.017	1.11×10^{10}	1×10^4	—	56
CuPc/BPPC	0.008	3.94×10^9	1×10^5	3.92	57
MoS_2-PAM	0.60	4.96×10^{11}	4×10^4	20.37	58
Ga_2O_3-EAP	3.1	1.42×10^{11}	31	4.5×10^4	59
Pentacene/C_{60}	0.025	2.0×10^{10}	1×10^5	5	60
$Cs_3Bi_2I_9$	0.003	1.6×10^{12}	100	—	61
CQD/ZnO	0.14	8.33×10^{12}	1×10^3	—	62
Polyaniline–ZnO	0.024	—	9.3×10^2	7.47	63

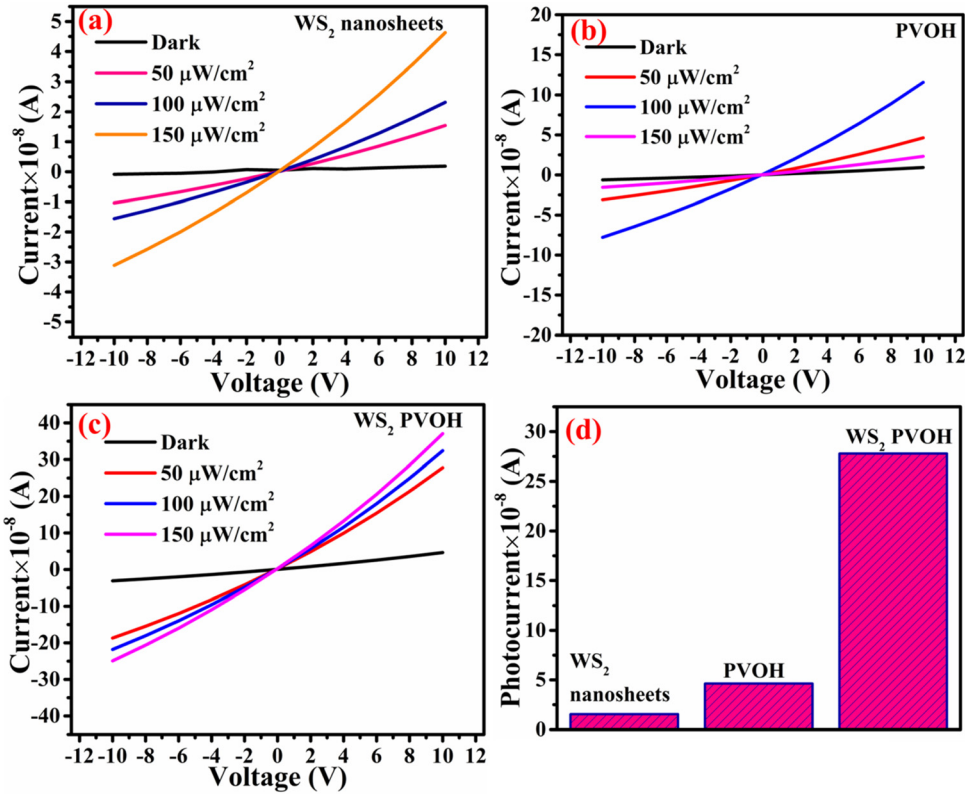

Fig. 7 Current–voltage characteristics of (a) WS_2 nanosheets, (b) PVOH and (c) WS_2 PVOH. (d) Comparison of the photocurrent in WS_2, PVOH and WS_2 PVOH at 10 V under an illumination intensity of 50 μW cm^{-2}.

and PVOH of 3.13×10^7, indicating that more carriers are collected at the electrodes in the material WS_2 PVOH.

$$R = \frac{I_{photo} - I_{dark}}{AP_{in}} \quad (9)$$

$$G = \frac{1240}{\lambda(nm)}R = \frac{I_{photo} - I_{dark}}{qf} \quad (10)$$

A photodetector's operation and properties can be determined by looking at its external quantum efficiency and detectivity characteristics. In contrast, detectivity describes the capacity of the photodetector to detect weak signals and can be calculated by relation (12). The collected charge carriers at the electrodes for each incoming photon are referred to as EQE (relation (11)).[55] The EQE values for the PVOH and WS_2 are found to be 3.12% and 1.77% but for the WS_2 PVOH device, it was observed to be 125.15%, which is much higher than that of both of its constituent parts, and as shown in Fig. 9(b), the EQE is higher than 100% indicating the photomultiplication phenomena in the WS_2 PVOH material.

$$\eta = \frac{I_{ph}/e}{P/h\nu} \quad (11)$$

$$D = \sqrt{\left(\frac{A}{2eI_{dark}}\right)}R \text{ Jones} \quad (12)$$

In contrast to noise equivalent power, which is defined as the observable optical power from its noise level, linear dynamic range (relation (13)) refers to the range of photodetector response to the input light. The LDR values for WS_2 nanosheets, PVOH and WS_2 PVOH are observed to be 2.07 dB, 12.32 dB and 22.259 dB, respectively. Noise equivalent power (relation (14)) for WS_2 PVOH is observed to be 1.67×10^{-7} W, which is much lower than that of both of its constituents, which means that it can detect much low optical signals than WS_2 nanosheets and PVOH. For the photodetector device, the response and recovery times are also crucial and are calculated by fitting relations (15) and (16). The response and recovery times for the WS_2 PVOH devices were found to be 1.158 s and 1.868 s, respectively, whereas the response and recovery times for WS_2 nanosheets were found to be the best as shown in Fig. 10(a).

$$\text{LDR} = 20 \log \frac{I_{photo}}{I_{dark}} \quad (13)$$

$$\text{NEP} = \frac{I_{dark}}{R}\text{Watt} \quad (14)$$

$$I(t) = I_{dark}(e^{-t/\tau_r}) \quad (15)$$

$$I(t) = I_{dark}(1-e^{-t/\tau_d}) \quad (16)$$

3.8 Density functional theory (DFT) approach

The DFT results are obtained by the simulation of PVOH, WS_2 and WS_2 PVOH. The molecules were created by using Gauss

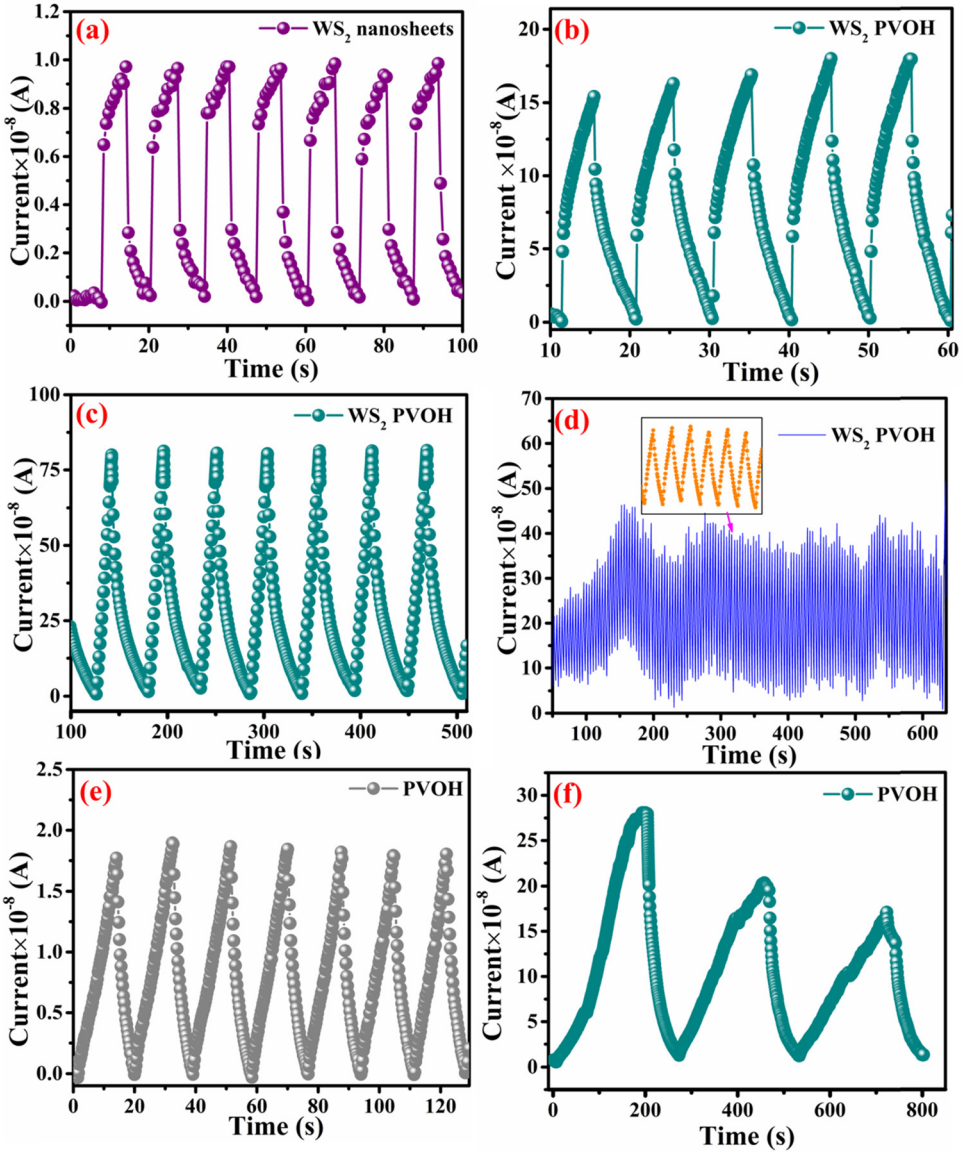

Fig. 8 (a) Transient photoresponse of WS_2 nanosheets. (b) Transient photoresponse of WS_2 PVOH with a small duration illumination pulse. (c) Transient photoresponse of WS_2 PVOH for a large duration illumination pulse. (d) Stability of the WS_2 PVOH photodetector device over 600 s. (e) Transient photoresponse of PVOH. (f) Transient photoresponse of PVOH for a large duration illumination pulse.

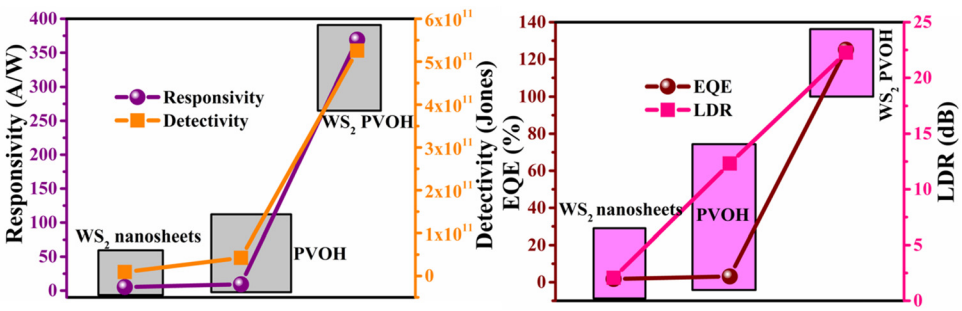

Fig. 9 (a) Responsivity and detectivity of the WS_2 PVOH photodetector device. (b) EQE and LDR of the WS_2 PVOH photodetector device.

View 05 and the Gaussian 09 program was used for the DFT calculations. The basis set of LanL2DZ was employed in this optimization process together with the ground state B3LYP density functional theory model.[64,65] The optimized structures

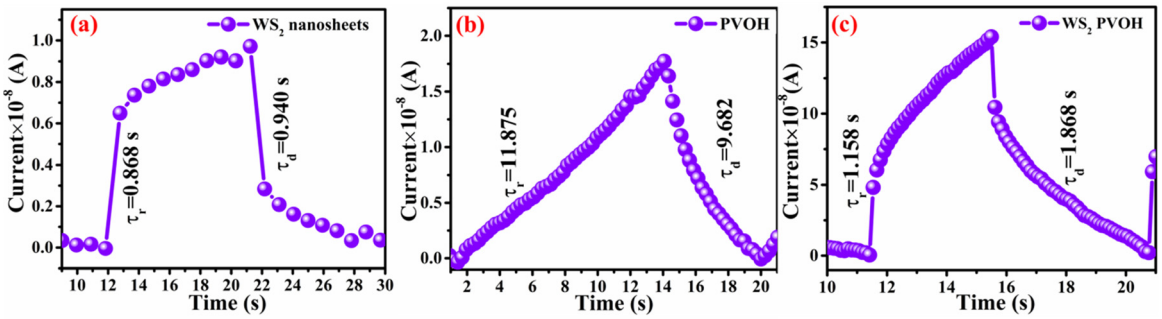

Fig. 10 Rise and decay time constants for (a) WS_2 nanosheets, (b) PVOH and (c) WS_2PVOH.

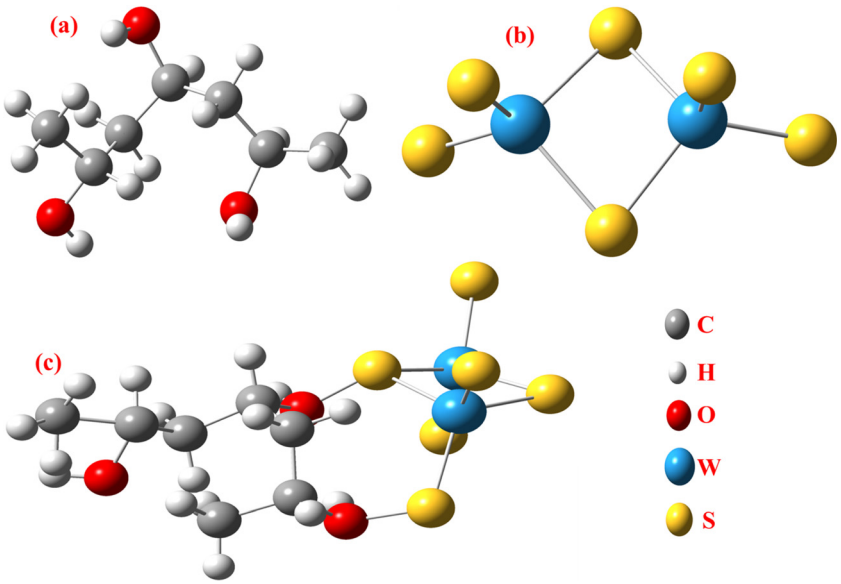

Fig. 11 Optimized structure of (a) PVOH, (b) WS_2 and (c) WS_2 PVOH.

of PVOH, WS_2 and WS_2 PVOH are presented in Fig. 11. Ning Xu *et al.*[66] also showed that the metallopolymer of WS_2 PVOH looks yellowish green, and is smooth with no obvious defects and excellent transparency. Certain S bare atoms that appeared at the edges of the nanosheets and could easily interact increased the force between PVOH and WS_2. On the other hand, the WS_2 addition disrupted the regularity of the PVOH polymer array. Evident improvement has been made in the composite's temperature properties, primarily because the physical barrier provided by the nanosheets can limit the thermal mobility of the polymer chain and inhibit heat conduction. These exposed S atoms produced a strong contact with the PVOH molecular chain, delaying the thermal breakdown of the composite material.[66] In the metallopolymeric system, there is contact between them because the W atom is in the WS_2 and the –OH functional group is in the PVOH matrix. There are certain electronic parameters, such as HOMO–LUMO gap (ΔE), electron affinity (EA), ionization potential (IP), electronegativity (μ), chemical potential (χ), chemical hardness (η), chemical softness (σ), and nucleophilicity index (ω), which can be calculated by relations (17)–(24),[67–69] to investigate the properties of the metallopolymeric system as presented in Table 3.

The HOMO is the highest molecular orbital that has any electrons. The second-highest energy orbital is the LUMO orbital (it will be empty). The LUMO is the place where an electron can be positioned or stimulated at the lowest energy. The lowest energy electronic excitation that a molecule is capable of experiencing is typically the energy difference between the HOMO and LUMO. We can learn about the wavelengths that the compound can absorb from this energy gap. In Fig. 12, the HOMO–LUMO gaps represented by red color show the positive phase and green color represents the negative phase. Both positive and negative phases are distributed with all molecules of WS_2 and PVOH but in WS_2 PVOH it is mostly distributed within WS_2 in both the HOMO and LUMO levels, which indicates that most of the electronic charge transfer takes place within WS_2 and PVOH provides more stability to the system. The HOMO levels of PVOH, WS_2 and WS_2 PVOH are found at −7.12, −7.70 and −6.26 eV, whereas the LUMO levels are found at 1.52, −5.94 and −4.14 eV, respectively; on the basis

Table 3 Electronic parameters of the simulation results

Materials	E_{HOMO} (eV)	E_{LUMO} (eV)	Band gap (eV)	Electron affinity (eV)	Ionization potential (eV)	Electronegativity (eV)	Chemical potential (eV)	Chemical hardness	Nucleophilicity index	Charge transfer (ΔN_{max})
PVOH	−7.12	1.52	8.65	−1.52	7.12	2.79	−2.79	4.32	−0.90	0.64
WS_2	−7.79	−5.94	1.85	5.94	7.79	6.86	−6.86	0.92	−25.48	7.42
WS_2 PVOH	−6.26	−4.14	2.11	4.14	6.26	5.20	−5.20	1.06	−12.79	4.91

of these results it can be concluded that it is easier to move an electron from the HOMO to LUMO levels because the HOMO level of PVOH and LUMO of WS_2 shift to lower levels of −7.12 eV and −5.94 eV. It can also be noted that the HOMO and LUMO levels of WS_2 are in between the PVOH HOMO to LUMO levels, which means that electrons travel from WS_2 to PVOH for the transition to a higher excited level, which can also be seen in the experimental results of photodetection; for example, two types of transitions are found: one fast rise or decay and a second slow rise or decay. The HOMO–LUMO gap was discovered to be 8.65 eV, 1.85 eV, and 2.11 eV for PVOH, WS_2, and WS_2 PVOH, according to the examination of the simulation findings. This tells us that when the WS_2 nanosheets are added to the PVOH matrix, the excitation energy or absorption energy reduces from pure WS_2 sheets and increases as compared to PVOH. Fig. 12 illustrates how the addition of WS_2 to the PVOH matrix altered the HOMO–LUMO gap energy. The chemical reactivity parameters based on the values of the HOMO and LUMO energies have been established.[70] Understanding the relationship between the HOMO and LUMO energy gaps is essential for defining the chemical reactivity and kinetic stability of polymers as well as understanding static molecular reactivity. The chemical reactivity of the molecule is fundamentally described by its ionization energy. The ionization energy can forecast the reactivity of compounds. A compound's stability is indicated by high ionization energy, whereas its reactivity is shown by low ionization energy.[71]

The results of the electron affinity test indicated that the accepted electrons might be bonded to a chemical structure. PVOH typically has an ionization potential of 9 eV. The electron affinity values show that when PVOH, WS_2, and WS_2 PVOH accept one electron to form a radical anion, they release, respectively, −1.52, 5.94, and 6.26 eV of energy. A lower electron affinity value means that the substance does not readily receive electrons. It follows that WS_2 can rapidly accept electrons from the environment in comparison to WS_2 PVOH. Absolute hardness and softness, which are inversely correlated, are essential properties. They also gauge a material's molecular stability, reactivity, and electron transfer resistance. The chemical hardness of PVOH, WS_2, and WS_2 PVOH is determined to be, respectively, 4.32, 0.92, and 1.06 eV. The chemical potential describes the propensity of electrons to escape an equilibrium solution. As the electronic chemical potential rises, the molecule becomes less stable or more reactive.[72] The highest chemical potential of −6.86 eV is detected for WS_2, whereas it is observed to be −2.79 eV and −5.20 eV for PVOH and WS_2 PVOH, respectively. This indicates that the WS_2 PVOH system is more stable than the WS_2 system. Energy stabilization occurs when a system picks up an extra electronic charge (ΔN) from its surroundings. The tendency of the electrophile to pick up an extra electronic charge driven by us as well as the system's resistance to exchanging electronic charge with the environment described by N_{max} are both included in the electrophilicity index. The charge transfer (ΔN) results of 7.42 reveal that WS_2 can exchange more electronic charge from the environment but at the same time the lower HOMO–LUMO gap exhibited lower stability, but after conjugating with PVOH, ΔN was found to be 4.91 which shows the higher electronic

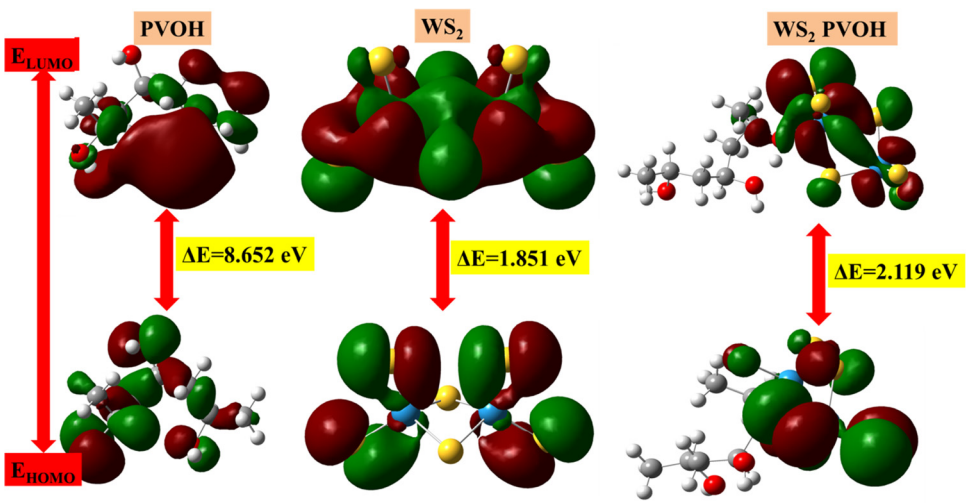

Fig. 12 HOMO–LUMO based energy gap in (a) PVOH, (b) WS_2 and (c) WS_2 PVOH.

change exchange capability with higher stability as compared to WS_2.

$$\text{HOMO–LUMO gap } (\Delta E) = E_{\text{LUMO}} - E_{\text{HOMO}} \quad (17)$$

$$\text{Electron affinity (EA)} = -E_{\text{LUMO}} \quad (18)$$

$$\text{Ionization potential (IP)} = -E_{\text{HOMO}} \quad (19)$$

$$\text{Electronegativity } (\mu) = -\left(\frac{E_{\text{HOMO}} + E_{\text{LUMO}}}{2}\right) \quad (20)$$

$$\text{Chemical potential } (\chi) = \left(\frac{E_{\text{HOMO}} + E_{\text{LUMO}}}{2}\right) \quad (21)$$

$$\text{Chemical hardness } (\eta) = \left(\frac{E_{\text{LUMO}} - E_{\text{HOMO}}}{2}\right) \quad (22)$$

$$\text{Nucleophilic index } (\omega) = -\frac{\mu^2}{2\eta} \quad (23)$$

$$\text{Charge transfer } (\Delta N_{\max}) = -\left(\frac{\mu}{\eta}\right) \quad (24)$$

4. Conclusion

It can be concluded from the above discussion that WS_2 nanosheets are successfully incorporated into the PVOH matrix, which can be used as a photodetector device. The semi-crystalline character is shown once the WS_2 nanosheets have been incorporated into the PVOH matrix. With a band gap of 3.51 eV, the UV-Visible absorbance measurements demonstrate that this material is particularly appropriate for UV light detection. This photodetector device exhibited the highest responsivity of 369.13 mA W^{-1} with a detectivity of 5.25×10^{11} Jones. As compared to PVOH, WS_2-incorporated PVOH shows better performance in terms of photodetector parameters. For the photodetector device based on WS_2 PVOH, the photodetector parameters revealed that this device is very useful for UV light detection. On the basis of DFT analysis, it can also be concluded that upon the incorporation of WS_2 nanosheets in the PVOH matrix, the HOMO–LUMO gap energy decreased to 2.11 eV as compared to the PVOH energy of 8.65 eV.

Conflicts of interest

There are no conflicts to declare.

Acknowledgements

Mr Arpit Verma and the corresponding author acknowledge the Uttar Pradesh Council of Science and Technology, Lucknow for financial assistance in the form of Project Ref. CST/D-2290. The authors are also thankful to USIC, BBAU, Lucknow for providing characterization facilities such as SEM, XRD, and FTIR.

References

1 J. Huang, L. Yan, S. Liu, L. Tao and B. Zhou, *Mater. Horiz.*, 2022, **9**, 1167–1195.
2 H. Michaels, I. Benesperi and M. Freitag, *Chem. Sci.*, 2021, **12**, 5002–5015.
3 Q. H. Wang, K. Kalantar-Zadeh, A. Kis, J. N. Coleman and M. S. Strano, *Nat. Nanotechnol.*, 2012, **7**, 699–712.
4 P. K. Khanna, P. Phalswal, H.-G. Rubahn and Y. K. Mishra, *Mater. Adv.*, 2022, **3**, 5672–5697.
5 A. Khunger, N. Kaur, Y. K. Mishra, G. R. Chaudhary and A. Kaushik, *Mater. Lett.*, 2021, **304**, 130656.
6 W. Zhang, C.-P. Chuu, J.-K. Huang, C.-H. Chen, M.-L. Tsai, Y.-H. Chang, C.-T. Liang, Y.-Z. Chen, Y.-L. Chueh and J.-H. He, *Sci. Rep.*, 2014, **4**, 1–8.
7 R. K. Tripathi, O. S. Panwar, I. Rawal, C. K. Dixit, A. Verma, P. Chaudhary, A. K. Srivastava and B. C. Yadav, *J. Mater. Sci.: Mater. Electron.*, 2021, **32**, 2535–2546.
8 A. Verma, P. Chaudhary, A. Singh, R. K. Tripathi and B. C. Yadav, *ACS Appl. Nano Mater.*, 2022, **5**, 4860–4874.
9 R. Wadhwa, A. V. Agrawal, D. Kushavah, A. Mushtaq, S. K. Pal and M. Kumar, *Appl. Surf. Sci.*, 2021, **569**, 150949.
10 P. Aggarwal, S. Kaushik, P. Bisht, M. Sharma, A. Singh, B. R. Mehta and R. Singh, *Cryst. Growth Des.*, 2022, **22**, 3206–3217.
11 J. S. Shaikh, N. S. Shaikh, S. Sabale, N. Parveen, S. P. Patil, Y. K. Mishra, P. Kanjanaboos, S. Praserthdam and C. D. Lokhande, *Mater. Today Chem.*, 2021, **21**, 100480.
12 N. Dong, Y. Li, Y. Feng, S. Zhang, X. Zhang, C. Chang, J. Fan, L. Zhang and J. Wang, *Sci. Rep.*, 2015, **5**, 1–10.
13 R. Wadhwa, A. V. Agrawal and M. Kumar, *J. Phys. D: Appl. Phys.*, 2021, **55**, 063002.
14 W. Song, Q. Liu, J. Chen, Z. Chen, X. He, Q. Zeng, S. Li, L. He, Z. Chen and X. Fang, *Small*, 2021, **17**, 2100439.
15 L. Britnell, R. V. Gorbachev, R. Jalil, B. D. Belle, F. Schedin, A. Mishchenko, T. Georgiou, M. I. Katsnelson, L. Eaves and S. V. Morozov, *Science*, 2012, **335**, 947–950.
16 A. K. Geim and I. V. Grigorieva, *Nature*, 2013, **499**, 419–425.
17 V. Chaudhary, N. Ashraf, M. Khalid, R. Walvekar, Y. Yang, A. Kaushik and Y. K. Mishra, *Adv. Funct. Mater.*, 2022, **32**, 2112913.
18 V. Chaudhary, A. K. Kaushik, H. Furukawa and A. Khosla, *ECS Sensors Plus*, 2022, **1**, 013601.
19 L. Shooshtari, S. Ghods, R. Mohammadpour and A. Esfandiar, *Sci. Rep.*, 2022, **12**, 1–14.
20 W. Zhu, T. Low, H. Wang, P. Ye and X. Duan, *2D Mater.*, 2019, **6**, 032004.
21 A. Singh, S. Sikarwar, A. Verma and B. C. Yadav, *Sens. Actuators, A*, 2021, **332**, 113127.
22 D. Jariwala, T. J. Marks and M. C. Hersam, *Nat. Mater.*, 2017, **16**, 170–181.
23 P. Chaudhary, A. Verma, A. Mishra, D. Yadav, K. Pal, B. C. Yadav, E. R. Kumar, K. B. Thapa, S. Mishra and D. K. Dwivedi, *Phys. E*, 2022, **139**, 115174.
24 A. Verma, U. Kumar, P. Chaudhary and B. C. Yadav, *Solid State Commun.*, 2022, **348**, 114723.

25 S. Cai, X. Xu, W. Yang, J. Chen and X. Fang, *Adv. Mater.*, 2019, **31**, 1808138.
26 A. Singh, A. Verma, B. C. Yadav and P. Chauhan, *Dalton Trans.*, 2022, **51**, 7864–7877.
27 D. Zhu, D. Ji, L. Li and W. Hu, *J. Mater. Chem. C*, 2022, **10**, 13312–13323.
28 L. Shi, Q. Liang, W. Wang, Y. Zhang, G. Li, T. Ji, Y. Hao and Y. Cui, *Nanomaterials*, 2018, **8**, 713.
29 Z. Zhong, K. Li, J. Zhang, L. Ying, R. Xie, G. Yu, F. Huang and Y. Cao, *ACS Appl. Mater. Interfaces*, 2019, **11**, 14208–14214.
30 M. Ahmadi, T. Wu and B. Hu, *Adv. Mater.*, 2017, **29**, 1605242.
31 J. Yang, J.-U. Lee and H. Cheong, *FlatChem*, 2017, **3**, 64–70.
32 W. Zhao, Z. Ghorannevis, K. K. Amara, J. R. Pang, M. Toh, X. Zhang, C. Kloc, P. H. Tan and G. Eda, *Nanoscale*, 2013, **5**, 9677–9683.
33 K.-G. Zhou, F. Withers, Y. Cao, S. Hu, G. Yu and C. Casiraghi, *ACS Nano*, 2014, **8**, 9914–9924.
34 A. Berkdemir, H. R. Gutiérrez, A. R. Botello-Méndez, N. Perea-López, A. L. Elías, C.-I. Chia, B. Wang, V. H. Crespi, F. López-Urías and J.-C. Charlier, *Sci. Rep.*, 2013, **3**, 1–8.
35 S. B. Aziz, I. Brevik, M. A. Brza, A. S. F. M. Asnawi, E. Dannoun, Y. M. Yusof, R. T. Abdulwahid, M. H. Hamsan, M. M. Nofal and M. F. Z. Kadir, *Materials*, 2020, **13**, 5030.
36 R. Ricciardi, F. Auriemma, C. De Rosa and F. Lauprêtre, *Macromolecules*, 2004, **37**, 1921–1927.
37 S. Sikarwar, B. C. Yadav, S. Singh, G. I. Dzhardimalieva, S. I. Pomogailo, N. D. Golubeva and A. D. Pomogailo, *Sens. Actuators, B*, 2016, **232**, 283–291.
38 P. Chaudhary, D. K. Maurya, A. Pandey, A. Verma, R. K. Tripathi, S. Kumar and B. C. Yadav, *Sens. Actuators, B*, 2022, **350**, 130818.
39 P. Rademeyer, D. Carugo, J. Y. Lee and E. Stride, *Lab Chip*, 2015, **15**, 417–428.
40 B. Lorber, F. Fischer, M. Bailly, H. Roy, D. J. B. Kern and M. B. Education, *Biochem. Mol. Biol. Educ.*, 2012, **40**, 372–382.
41 A. Verma, D. Yadav, A. Singh, M. Gupta, K. B. Thapa and B. C. Yadav, *Sens. Actuators, B*, 2022, **361**, 131708.
42 S. Bhattacharjee, *J. Controlled Release*, 2016, **235**, 337–351.
43 V. R. Patel and Y. K. Agrawal, *J. Adv. Pharm. Technol. Res.*, 2011, **2**, 81.
44 A. Singh, P. Chauhan, A. Verma and B. Chandra Yadav, *Sustainable Energy Fuels*, 2023, **7**, 131–143.
45 S. F. Alvarado, P. F. Seidler, D. G. Lidzey and D. D. C. Bradley, *Phys. Rev. Lett.*, 1998, **81**, 1082.
46 L. Li, F. Zhang, J. Wang, Q. An, Q. Sun, W. Wang, J. Zhang and F. Teng, *Sci. Rep.*, 2015, **5**, 1–7.
47 A. Verma, P. Chaudhary, R. K. Tripathi and B. C. Yadav, *Mater. Adv.*, 2022, **3**, 3994–4005.
48 Z. Zhang and J. T. Yates Jr, *Chem. Rev.*, 2012, **112**, 5520–5551.
49 B. D. Boruah, *Nanoscale Adv.*, 2019, **1**, 2059–2085.
50 R. Raj, P. Lohia, D. Dwivedi, A. Verma and B. C. Yadav, *J. Mater. Sci.: Mater. Electron.*, 2022, 1–10.
51 B. Philippa, R. White and A. Pivrikas, *Appl. Phys. Lett.*, 2016, **109**, 153301.
52 A. Verma, P. Chaudhary, R. K. Tripathi and B. C. Yadav, *Sens. Actuators, A*, 2021, **321**, 112600.
53 A. Verma, P. Chaudhary, R. K. Tripathi, A. Singh and B. C. Yadav, *J. Inorg. Organomet. Polym. Mater.*, 2022, **32**, 2807–2826.
54 M. Zhu, Z. Zhao, Y. Fang, C. Fang, Z. Weng, W. Lei, S. B. Shafie and M. N. Mohtar, *Appl. Phys. A: Mater. Sci. Process.*, 2021, **127**, 1–8.
55 C. Gautam, A. Verma, P. Chaudhary and B. C. Yadav, *Opt. Mater.*, 2022, **123**, 111860.
56 D. Kannichankandy, P. M. Pataniya, C. K. Zankat, M. Tannarana, V. M. Pathak, G. K. Solanki and K. D. Patel, *Appl. Surf. Sci.*, 2020, **524**, 146589.
57 D. Nath, P. Dey, A. M. Joseph, J. K. Rakshit and J. N. Roy, *Opt. Mater.*, 2020, **108**, 110371.
58 A. Verma, P. Chaudhary, R. K. Tripathi and B. C. Yadav, *Sustainable Energy Fuels*, 2021, **5**, 1394–1405.
59 K. Arora, K. Kaur and M. Kumar, *ACS Appl. Electron. Mater.*, 2021, **3**, 1852–1863.
60 D. Nath, P. Dey, A. M. Joseph, J. K. Rakshit and J. N. Roy, *Opt. Laser Technol.*, 2020, **131**, 106393.
61 A. A. Hussain, *ACS Appl. Mater. Interfaces*, 2020, **12**, 46317–46329.
62 S.-W. Lee, K.-J. Choi, B.-H. Kang, J.-S. Lee, S.-W. Kim, J.-B. Kwon, S.-A. Gopalan, J.-H. Bae, E.-S. Kim and D.-H. Kwon, *Org. Electron.*, 2016, **39**, 250–257.
63 R. A. Talib, M. Abdullah, H. S. Al-Salman, S. M. Mohammad and N. K. Allam, *Mater. Chem. Phys.*, 2016, **181**, 7–11.
64 A. Frisch, *Gaussian 09*, Wallingford, USA, 2009, vol. 470.
65 G. J. Zheng, L. Sonnenberg, M. Hada, M. Ehara, K. Toyota, R. Fukuda, J. Hasegawa, M. Ishida, T. Nakajima and Y. Honda, *Gaussian 09*, *Gaussian Inc.*, *Wallingford CT*, 2009.
66 N. Xu, J. Chen, Q. Wei, E. Ding, X. Zeng, F. Xue, N. Zhang and J. Shang, *J. Appl. Polym. Sci.*, 2020, **137**, 48487.
67 U. Kumar, H.-W. Hsieh, Y.-C. Liu, Z.-Y. Deng, K.-L. Chen, W.-M. Huang and C.-H. Wu, *ACS Appl. Mater. Interfaces*, 2022, **14**(28), 32279–32288.
68 U. Kumar, Y.-H. Yang, Z.-Y. Deng, M.-W. Lee, W.-M. Huang and C.-H. Wu, *Sens. Actuators, B*, 2022, **353**, 131192.
69 S. Singh, P. Yadav, M. K. Gupta, G. I. Dzhardimalieva, J. Yoon, C. Maiti and B. C. Yadav, *Sens. Actuators, B*, 2022, **359**, 131573.
70 S. Sikarwar, A. Pandey, A. Singh, B. C. Yadav, I. E. Uflyand and G. I. Dzhardimalieva, *Mater. Sci. Eng., B*, 2022, **283**, 115813.
71 G. Maheswari and R. V. Williams, *Int. J. Res. Anal. Rev.*, 2019, **6**, 513–528.
72 R. Molavi, R. Safaiee and M. H. Sheikhi, *Phys. Chem. Chem. Phys.*, 2020, **22**, 14889–14899.